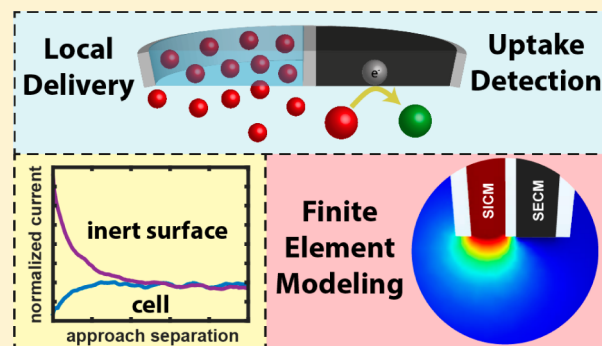


## Quantitative Visualization of Molecular Delivery and Uptake at Living Cells with Self-Referencing Scanning Ion Conductance Microscopy-Scanning Electrochemical Microscopy

Ashley Page,<sup>†,‡,§</sup> Minkyung Kang,<sup>†</sup> Alexander Armitstead,<sup>†</sup> David Perry,<sup>†,‡</sup> and Patrick R. Unwin<sup>\*,†</sup><sup>†</sup>Department of Chemistry and <sup>‡</sup>MOAC Doctoral Training Centre, University of Warwick, Coventry, CV4 7AL, United Kingdom

## S Supporting Information

**ABSTRACT:** A multifunctional dual-channel scanning probe nanopipet that enables simultaneous scanning ion conductance microscopy (SICM) and scanning electrochemical microscopy (SECM) measurements is demonstrated to have powerful new capabilities for spatially mapping the uptake of molecules of interest at living cells. One barrel of the probe is filled with electrolyte and the molecules of interest and is open to the bulk solution for both topographical feedback and local delivery to a target interface, while a solid carbon electrode in the other barrel measures the local concentration and flux of the delivered molecules. This setup allows differentiation in molecular uptake rate across several regions of single cells with individual measurements at nanoscale resolution. Further, operating in a “hopping mode”, where the probe is translated toward the interface (cell) at each point allows self-referencing to be employed, in which the carbon electrode response is calibrated at each and every pixel in bulk for comparison to the measurement near the surface. This is particularly important for measurements in living systems where an electrode response may change over time. Finite element method (FEM) modeling places the technique on a quantitative footing to allow the response of the carbon electrode and local delivery rates to be quantified. The technique is extremely versatile, with the local delivery of molecules highly tunable via control of the SICM bias to promote or restrict migration from the pipet orifice. It is expected to have a myriad of applications from drug delivery to screening catalysts.



All living cells, irrespective of whether they are plant, animal, or bacterial, are continuously exchanging molecules with their extracellular environment. These molecules can range from the small diatomic oxygen ( $O_2$ ) used in cellular respiration,<sup>1–3</sup> to cytokines,<sup>4</sup> signaling proteins used for intercellular communication that can be 20 kDa or larger in size. The passage of any species from the extracellular to the intracellular domain or vice versa is dependent on a host of factors, including molecule size and charge,<sup>5,6</sup> physiological conditions and environment,<sup>7</sup> relative concentrations inside and outside of the cell,<sup>8</sup> and the presence of suitable membrane proteins if assisted transport is necessary.<sup>9,10</sup> The dependence of uptake on such a wide variety of factors, and the fact that uptake is a complex process involving mass transport (diffusion) and interfacial (membrane) processes, imposes critical requirements on analytical techniques if key details on uptake are to be revealed. Although cell uptake measurements are an essential aspect of new drug development, current methods often use bulk cytotoxicity assays and, at best, whole single cell measurements to ascertain the efficacy of a drug.<sup>11–14</sup>

Scanning electrochemical probe microscopies (SEPMs) have great potential to increase the precision of cellular uptake measurements, particularly as the production of functional nanoscale probes is becoming easier.<sup>15</sup> Hitherto, scanning

electrochemical microscopy (SECM)<sup>16</sup> and scanning ion conductance microscopy (SICM)<sup>17</sup> have been the main SEPMs used for cell imaging. SICM has mainly been used for high-resolution topographical imaging,<sup>18,19</sup> while SECM has found considerable application for imaging a variety of processes at living cells.<sup>20,21</sup> However, measurements of cell permeability with SECM are somewhat scarce<sup>22,23</sup> and challenging, because existing detection schemes, such as the induced transfer mode,<sup>24</sup> require careful deconvolution of topography and induced transfer (interfacial kinetics). Furthermore, this mode involves the “extraction” of analyte by diffusion from within a cell or tissue, which may not give an accurate measurement of permeability if the analyte is consumed or irreversibly bound inside the cell.

Here, we report a new method combining SICM and SECM probes to determine the topography of a substrate and cell permeability (molecular uptake) simultaneously and in real time. While integrated electrodes have previously been used to monitor molecular efflux from micropipets,<sup>25,26</sup> they have not been used to monitor uptake at cells and our work greatly

Received: November 22, 2016

Accepted: January 24, 2017

Published: January 24, 2017



develops the capability of SICM-SECM,<sup>27–30</sup> which has recently been applied to model substrates<sup>27,28,31</sup> and electrocatalysis at nanoparticles.<sup>29,32</sup>

The approach makes use of SICM-SECM as a multifunctional tool to spatially resolve the uptake of a molecule of interest to a single cell (SECM channel), while reliably positioning the probe at a defined distance from the interface for delivery and topography mapping (SICM channel). The analyte of interest is delivered to the cell in a defined and local manner. This is advantageous compared to the analyte being in bulk solution, because (i) it allows the detection of uptake; (ii) the cell is only dosed transiently with the analyte, which reduces potential toxicity issues; and (iii) the response of the SECM and SICM channels can be calibrated at each and every pixel. Furthermore, the migration and thus delivery of molecules can be controlled by the polarity and magnitude of the applied SICM bias. As a proof of concept the uptake of the well-characterized redox mediator hexammineruthenium(III),  $[\text{Ru}(\text{NH}_3)_6]^{3+}$ , into *Zea mays* root hair cells has been studied. The technique is comfortably able to differentiate between uptake over the cell and the lack of uptake over glass and is further able to distinguish heterogeneities in uptake rates across different regions of cells. Interestingly, the rates correlate qualitatively to earlier measurements of membrane surface charge.<sup>33</sup> This subcellular resolution is a significant improvement on previous uptake assays and provides a roadmap to further refine the spatial and kinetic resolution. An important aspect of the method is that the probe response can be predicted with finite element method (FEM) modeling to provide a robust platform on which the cellular uptake of any electroactive molecule of interest could potentially be studied at the nanoscale, and the method could be applied to many other types of interfaces in addition to cells.

## EXPERIMENTAL SECTION

**Solutions.** Milli-Q reagent grade water (resistivity  $\sim 18.2$  M $\Omega$  cm at 25  $^{\circ}\text{C}$ ) was used for all solutions. A solution of 10 mM KCl (Sigma-Aldrich, pH 6.5) was prepared and used for the bulk solution in all experiments. A solution of 10 mM hexammineruthenium(III) chloride (Sigma-Aldrich) and 10 mM KCl was prepared and used in the SICM barrel for all experiments.

**Substrate Preparation.** *Zea mays* seeds (Avenir, Syngenta) were germinated between two layers of damp paper towel at 25  $^{\circ}\text{C}$  for 4 days. This provided a root of approximately 20 mm length with a dense layer of root hair cells. The corn roots were then attached to a glass-bottomed Petri dish (3512, WillcoWells) using SPM adhesive tabs (Agar Scientific) away from the area being imaged.

**Probe Fabrication.** The fabrication of the nanoprobes used for SICM-SECM uptake mapping involved a multistage process. First, a dual-barrel quartz “theta” capillary (o.d. 1.2 mm, i.d. 0.9 mm, Friedrich and Dimmock) was pulled to a sharp point of  $\sim 150$  nm total diameter using a laser puller (P-2000, Sutter Instruments). One of the barrels was sealed with “Blu-Tack” (Bostik) before butane was flowed down the other barrel in an argon atmosphere (Figure 1a). The probe was heated to pyrolytically deposit carbon within the barrel,<sup>31,34</sup> with the butane torch moved laterally, starting from beyond the end of the probe, over the tip, and along the probe body. The burn time was typically 3 s at the tip and 10 s on the probe body to ensure that a thick layer of carbon was deposited.

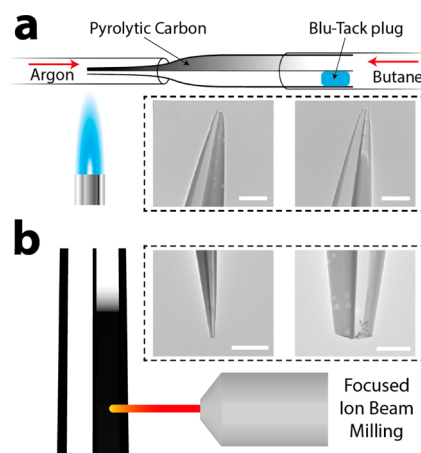


**Figure 1.** Fabrication of dual-barrel nanoprobes for use in SICM-SECM. (a) Carbon was deposited in one barrel of the probe via the pyrolysis of butane (SECM) while the other was kept open (SICM). Inset transmission electron microscopy (TEM) images show an example of both complete (left) and incomplete (right) carbon deposition. Scale bar in both micrographs is 500 nm. (b) The probe diameter was regulated using focused ion beam (FIB) milling. Inset TEM images show a probe with scale bars of 5  $\mu\text{m}$  (left) and 500 nm (right) after FIB milling.

An electrical connection to the SECM electrode was established by inserting a copper wire through the top end of the pipet barrel to make a back contact with the carbon layer. A transmission electron microscope (TEM, JEOL 2000FX) was used to investigate the carbon deposit (see inset micrographs, Figure 1a). The carbon deposit could be conformal to the end (left side image) or result in a recessed layer (right-hand image). To avoid complications arising from an irregular SECM tip geometry, the overall probe diameter was increased to 500 nm using focused ion beam (FIB) milling (JEOL 4500) to ensure consistent probe geometry with a flush carbon electrode (Figure 1b), the response of which could be more accurately modeled. Ag/AgCl quasi-reference counter electrodes (QRCEs), comprising AgCl-coated Ag wire,<sup>35,36</sup> were used in the open barrel of the probe and in the bulk solution for SICM feedback (topographical imaging).

**Instrumentation.** The SICM-SECM setup was built on the stage of an inverted optical microscope (Axiovert 40 CFL, Zeiss) to facilitate the positioning of the nanoprobe relative to the substrate. Probe movement normal to the substrate was controlled using a piezoelectric positioning stage with a travel range of 38  $\mu\text{m}$  (P-753-3CD, Physik Instrumente), while fine lateral movement of the substrate for XY positioning was achieved using a two-axis piezoelectric positioning system with a travel range of 300  $\mu\text{m}$  (Nano-BioS300, Mad City Laboratories, Inc.). Instrumentation control and data collection was achieved using a custom-written LabVIEW (2013, National Instruments) program through an FPGA card (NI PCIe-7852R, National Instruments) and custom-built current amplifiers.

**Simultaneous Topography and Uptake Mapping.** To simultaneously image topography and uptake, the SICM-SECM probe was approached toward the surface at 2  $\mu\text{m s}^{-1}$  (for small area scans) and 3  $\mu\text{m s}^{-1}$  for larger scans (specified herein) until the ionic (SICM) current dropped by 1.5%, compared to the bulk value at each pixel. This was the feedback threshold used throughout. A hopping regime<sup>28,37</sup> was used to permit a quantifiable measurement to be taken at each pixel. The bias between the two QRCEs used for SICM feedback was 0.2 V

with the positive bias applied at the QRCE in the SICM barrel. A bias of  $-0.4$  V was applied to the carbon electrode with respect to the QRCE in bulk solution so as to reduce  $[\text{Ru}(\text{NH}_3)_6]^{3+}$  to  $[\text{Ru}(\text{NH}_3)_6]^{2+}$  at a transport-limited rate. The height of the substrate at each pixel was taken from the  $z$ -position at the point of closest approach based on the SICM response. The normalized SECM current response was calculated by dividing the faradaic reduction current value at the surface by that in bulk at the same pixel. The use of self-referencing data collection was extremely powerful, allowing the response of the probe to be recalibrated at every point in the scan.

**Finite Element Method (FEM) Simulations.** 3D FEM simulations were performed in COMSOL Multiphysics (v5.2) using the transport of diluted species and electrostatics modules. The dimensions of the probe for the simulation were taken from TEM micrographs.<sup>38</sup> The pipet was simulated as a double-barrel eccentric extruded cone with a total semimajor axis of 250 nm at the end of the pipet and a major axis of 160 nm for each of the two barrels. The height of the pipet simulated was 5  $\mu\text{m}$  with an inner cone angle of  $4.9^\circ$ . A series of steady-state simulations were carried out at different probe-substrate separations, with a bias of  $+0.2$  V in the pipet with respect to bulk, from which a working distance of 120 nm was determined from the drop in ionic current to the experimental feedback threshold. This separation was then used for further steady-state simulations with the probe positioned over surfaces with different uptake kinetics at the substrate boundary (first order heterogeneous rate constants,  $k$ , ranging from  $1 \times 10^{-5}$  to  $1000 \text{ cm s}^{-1}$ , see eq 1).

$$\text{flux} = -k[\text{Ru}(\text{NH}_3)_6]^{3+} \quad (1)$$

A  $[\text{Ru}(\text{NH}_3)_6]^{3+}$  concentration of 0 mM was applied to the boundary of the SECM electrode (diffusion-limited detection by reduction). Further details of all simulations, including the system of differential equations solved and all boundary conditions can be found in the [Supporting Information](#), section SI-1.

## RESULTS AND DISCUSSION

**Operational Principle.** The use of a dual-barrel nanoprobe for the quantitative detection of cellular uptake is conditional on an intimate understanding of two well established scanning probe techniques: SICM and SECM. As highlighted in the introduction, SICM utilizes the ionic current between two Ag/AgCl QRCEs, one in the probe and one in the bulk solution, as a feedback signal.<sup>39</sup> This current is dependent on the resistance in the system, which in bulk solution is determined almost exclusively by the aperture of the nanopipet, as the most resistive component.<sup>40</sup> However, as the probe approaches a surface (closer than one probe diameter) the system resistance increases as ion migration between the pipet and bulk solution is hindered by the surface. The corresponding decrease in current can therefore be used to set, and determine, the probe-substrate separation and hence measure the topography of the substrate with a resolution on the same scale as the probe opening.<sup>40</sup> Note that for the probe sizes, distances, and electrolyte concentrations used herein, the SICM current is immune to rectification effects.<sup>41–43</sup> SECM uses a solid micro- or nanoelectrode to probe the local concentration (or flux) of an electroactive species of interest. A potential is applied to the

electrode to either oxidize or reduce the desired molecule, with the resulting faradaic current used to obtain flux information.

One QRCE was in the open (electrolyte-filled) barrel of the probe while another was in bulk, with a potential,  $V_1$ , applied between the two. The carbon electrode was connected to an offset electrometer that allowed the variation of the applied potential,  $V_2 - V_1$ , without affecting the bias used for SICM (Figure 2a). Both the bulk solution and the electrolyte channel

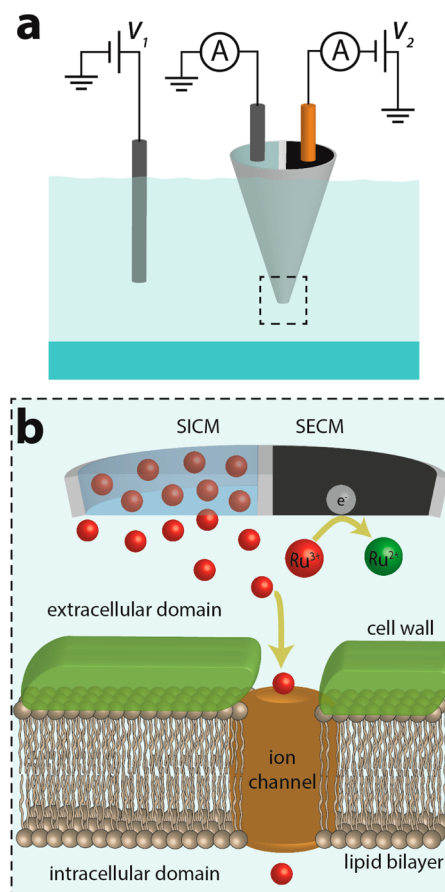


**Figure 2.** SICM-SECM experimental setup for the investigation of cellular uptake. (a) The current flowing between two Ag/AgCl QRCEs, one in bulk and one in the open channel of the probe, with an applied bias,  $V_1$ , used for topographical feedback in an SICM configuration. The carbon electrode used to measure the local concentration of the species is at a bias  $V_2 - V_1$ . (b) Schematic showing the diffusion-migration of  $[\text{Ru}(\text{NH}_3)_6]^{3+}$  from the SICM barrel into the near cell region. The current due to the reduction of  $[\text{Ru}(\text{NH}_3)_6]^{3+}$  at the SECM channel is monitored on approach of the probe to the surface and compared to the steady-state bulk current response to quantify uptake rates. It should be noted that transport via an ion channel is just one of many possible membrane transport mechanisms and is depicted herein for illustrative purposes.

of the probe contained 10 mM KCl. The molecule of interest (henceforth known as the “analyte”), was hexaammineruthenium(III) ( $[\text{Ru}(\text{NH}_3)_6]^{3+}$ ) as the chloride salt at a concentration of 10 mM, which was only in the electrolyte-filled barrel of the nanopipet. There was thus a concentration gradient of this species established around the tip of the probe and the transport of analyte from the open channel to the face of the carbon electrode determined the SECM current signal observed. It is worth noting that while there are interdependent electrochemical and transport processes at the



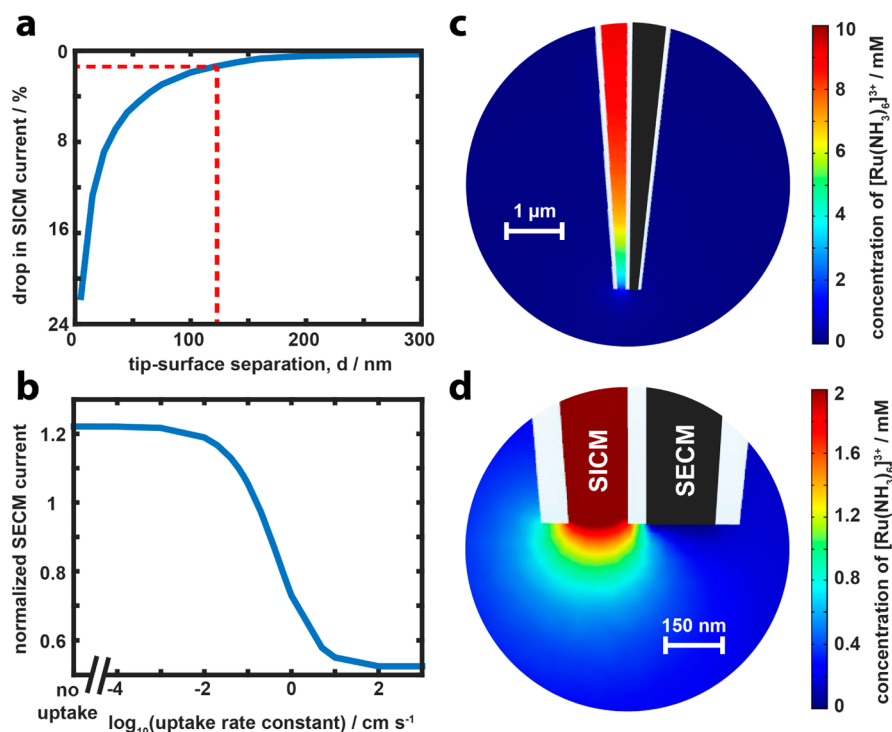


**Figure 3.** Finite element method (FEM) modeling of the SICM-SECM uptake system. (a) Simulated SICM approach curve (current vs distance) to a surface of zero uptake with a probe of the same geometry as used experimentally, with electrochemistry switched on at the SECM channel. The current data are plotted as the percentage drop in ionic current from the bulk value ( $\sim 850$  pA). The experimental threshold (red line in part a) was used to determine a working distance at which steady-state simulations (b) were carried out to calibrate the normalized SECM current as a function of the uptake rate constant at the surface. The normalized SECM current is the value at  $d = 120$  nm divided by that with the probe in bulk solution ( $\sim 10$  pA). (c and d) Concentration of  $[\text{Ru}(\text{NH}_3)_6]^{3+}$  at steady state with initial concentrations of 10 mM in the SICM barrel and 0 mM in bulk.

two channels, this interdependence is also treated in the simulations, with all simulations carried out with both the SICM and SECM channels “on” and both  $V_1$  and  $V_2$  held constant throughout.

Figure 2b is a schematic of an SICM-SECM probe near to a root hair cell. As  $[\text{Ru}(\text{NH}_3)_6]^{3+}$  molecules are taken across the membrane it can be seen that, for a fixed probe-substrate separation, the SECM signal would be lower at this substrate than at a completely solid (impermeable) surface, where  $[\text{Ru}(\text{NH}_3)_6]^{3+}$  would be partly trapped (hindered diffusion/migration) between the electrode and the surface. A specific normalized SECM current value (the ratio of the SECM current at the point of closest approach and the SECM current in bulk) thus corresponds to a specific level of uptake at the interface, as discussed in the next section.

**FEM Simulations.** FEM simulations of an SICM-SECM nanopipet (see Supporting Information, section SI-1 for full details) approaching a surface of zero uptake allowed the determination of a probe-substrate separation of 120 nm based on the 1.5% decrease of SICM current as the threshold used for the studies herein (Figure 3a). Further simulations were carried out with the probe at 120 nm above surfaces with varying analyte uptake rates, ranging from no uptake to a rate constant,  $k$ , of  $1000 \text{ cm s}^{-1}$  (see eq 1 above). Normalizing the steady-state SECM current values from these simulations to the value with the probe in bulk solution,  $10 \mu\text{m}$  away from the surface, generated a calibration curve of normalized SECM current versus uptake rate constant for the quantitative estimation of uptake kinetics to a given surface (Figure 3b). It can be seen that this technique has a wide dynamic window and is sensitive to rate constants from about  $0.01 \text{ cm s}^{-1}$  to  $10 \text{ cm s}^{-1}$ . This is a

positive feature of the method. On the other hand, accurate measurements require that the SECM channel current can be determined with high precision, which is why self-referencing is important, as we show herein.

An investigation was carried out into whether or not the uptake rate constant at the surface would influence the SICM current signal and thus the probe-substrate separation, the results of which are presented in Section SI-2 of the Supporting Information. For the uptake rate constants observed in this study, and the tip-substrate separation used, the flux of  $[\text{Ru}(\text{NH}_3)_6]^{3+}$  did not have a significant effect on the SICM current, with a small decrease predicted that was comparable to the noise of the SICM current measured experimentally. However, for a system where the uptake rate constant was higher (above  $1 \text{ cm s}^{-1}$ ), the probe-substrate separation could be influenced by the uptake of the analyte. This issue could be countered by employing an iterative approach in which both the separation and the uptake rate constant would be determined simultaneously over several rounds of simulations.

Experimentally the probe was retracted  $15 \mu\text{m}$  and this tip-substrate separation and that used in the simulations ( $10 \mu\text{m}$ ) are sufficient to represent bulk solution. The use of steady-state simulations is justified as the SECM response was the same at approach rates at least 5 times faster than those used experimentally, meaning that at any given point in the approach, the SECM current can be assumed to be at steady state. This is because the time to steady state at a nanoscale electrode is very short (see the Supporting Information, section SI-3 for further justification of steady-state simulations). It should be noted that for all simulations of the SECM current, the SICM bias ( $+0.2 \text{ V}$  at the QRCE in the probe) was applied,

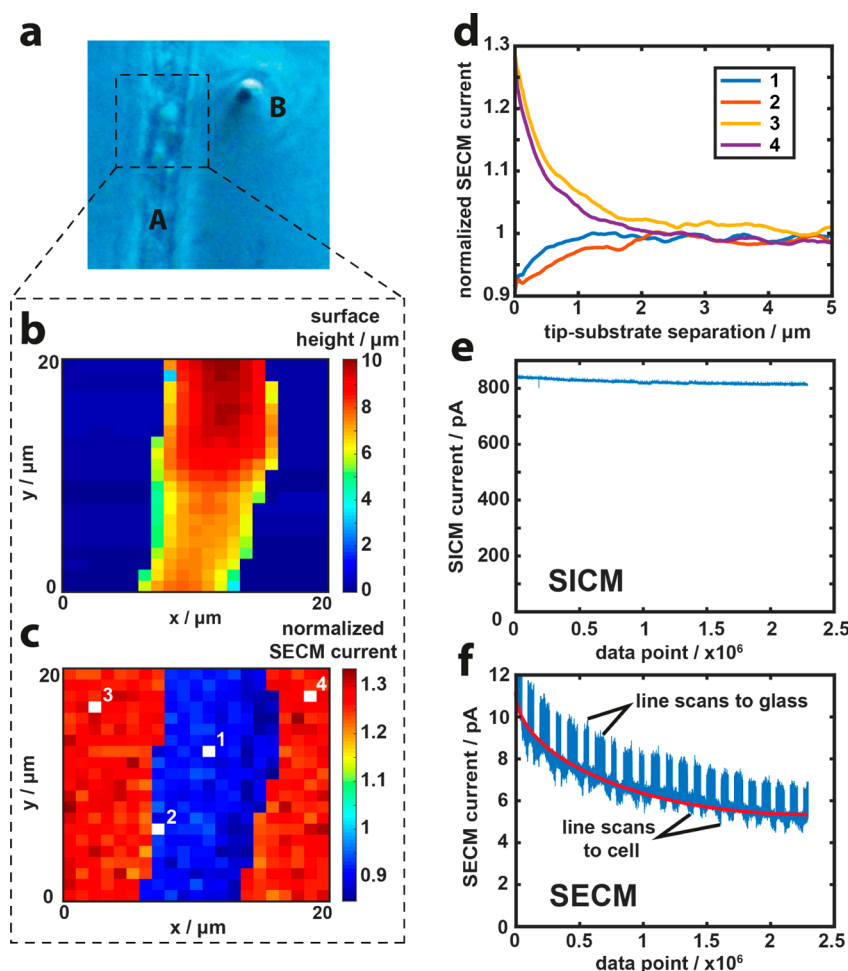


**Figure 4.** SICM-SECM topographical and  $[\text{Ru}(\text{NH}_3)_6]^{3+}$  uptake mapping of a *Zea mays* root hair cell on a glass substrate. (a) Optical image of the scanned root hair cell (A) on a glass support with the end of the probe also visible (B); scan area denoted by the dashed rectangle. (b) Substrate topography extracted from the z-position at the point of closest approach. (c) Normalized SECM current map showing the difference in uptake between glass substrate (zero uptake) and the root hair cell. "Normalized current" is the ratio of the  $[\text{Ru}(\text{NH}_3)_6]^{3+}$  steady-state limiting reduction current at the point of closest approach to the reduction current in bulk. Individual experimental approach curves from the scan in part c are shown in part d, at the four positions numbered. SICM (e) and SECM (f) currents across the entirety of the scan (400 separate approach curves) demonstrate minor current drift for SICM, but some effect for SECM, making the self-referencing approach essential. The red line in part f shows the trend in bulk SECM current, ignoring the approaches to either the cell or the glass.

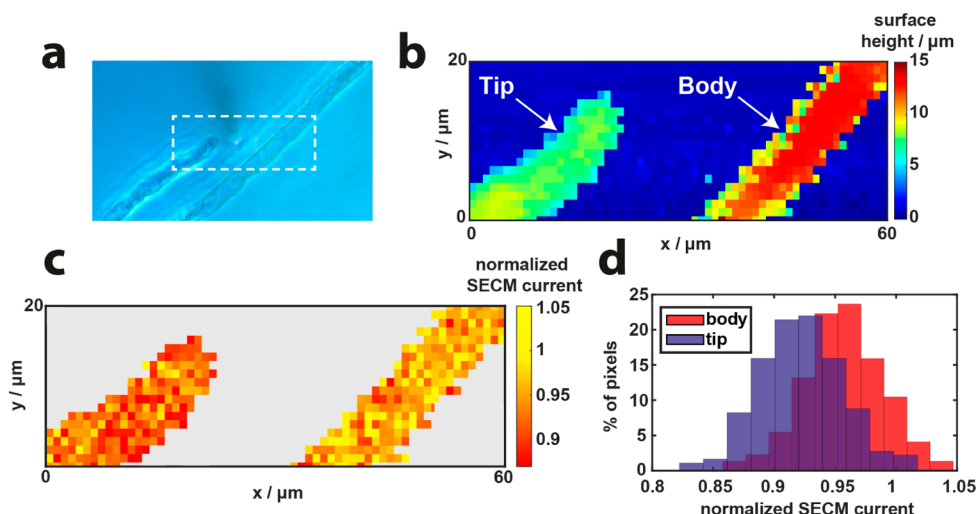
to imitate precisely the migration (as well as diffusion) of the  $[\text{Ru}(\text{NH}_3)_6]^{3+}$  that occurs in the experiments.

Figure 3c shows the steady-state concentration profile of  $[\text{Ru}(\text{NH}_3)_6]^{3+}$  with initial conditions mimicking those used experimentally, with the probe in bulk solution, and bias of +0.2 V vs the bulk QRCE applied in the SICM tip. The concentration at the nanopipet orifice is around 2 mM, one-fifth of the bulk nanopipet concentration of 10 mM. This difference is noteworthy when using nanopipets for local delivery, particularly drug delivery, as it is important to carefully dose the sample with a well-defined quantity (flux). A close-up of the end of the probe (Figure 3d) shows a departure from the expected hemispherical concentration profile at the end of the SICM barrel,<sup>44</sup> with the reduction of the  $[\text{Ru}(\text{NH}_3)_6]^{3+}$  to  $[\text{Ru}(\text{NH}_3)_6]^{2+}$  at the carbon electrode modifying the shape on the side closest to the solid amperometric sensor.

**Validation of SICM-SECM for Uptake Mapping.** As a proof-of-concept system for spatially resolved uptake mapping, a surface of reasonably high expected uptake (*Zea mays* root hair cells, see optical micrograph in Figure 4a) was imaged on a glass substrate (no expected uptake) in 10 mM KCl (pH 6.5).

Figure 4b,c show a typical pair of simultaneously collected topography and normalized SECM current maps of a root hair cell on a glass substrate. The height of the cell varies from 7 to 10  $\mu\text{m}$ , as it is not fully adhered to the surface,<sup>33</sup> and the steep drop off at the edges of the cell suggests a cylindrical morphology, consistent with previous work.<sup>33</sup>

The normalized SECM current map (Figure 4c) displays a very clear distinction between the behavior of the SECM channel over the root hair cell and the glass, with a pixel-perfect correlation with the topography map in Figure 4b, i.e., at every pixel the SECM response was consistent with the probe approaching the glass or cell (as indicated by topography). As mentioned above (Figure 3c), normalized SECM current values greater than 1 mean that the SECM current is higher close to the surface than in bulk. This is always observed over the glass substrate (typical value  $\sim 1.25$ ) and is caused by the hindered diffusion/migration of ions away from the end of the probe. A value of normalized SECM current lower than 1.25 corresponds to uptake by the sample. The values across the cell are similar, with an average value of  $0.91 \pm 0.02$ , suggesting a high uptake rate constant of  $0.31 \pm 0.03 \text{ cm s}^{-1}$  over the cell



**Figure 5.** SICM-SECM topographical and  $[\text{Ru}(\text{NH}_3)_6]^{3+}$  uptake mapping of two regions of a single *Zea mays* root hair cell. (a) Optical image of the scanned root hair cell; scan area denoted by the dashed rectangle. (b) Substrate topography extracted from the  $z$ -position at the point of closest approach from the SICM channel. (c) Normalized SECM current map showing a clear difference in uptake between the root hair cell body (higher current, lower uptake) and the root hair cell tip (lower current, higher uptake). “Normalized current” is the ratio of the  $[\text{Ru}(\text{NH}_3)_6]^{3+}$  reduction current at the point of closest approach to the same reduction current in bulk. (d) Histograms of the normalized SECM current across the two different regions of the root hair cell, “tip” and “body” (see part b).

surface (Figure 3c). Individual approach curves of the SECM current taken from the scan in Figure 4c are shown in Figure 4d, to illustrate the consistency of the measurements in different areas of the cell and different areas of the glass, and the contrasting behavior in the approach curve between the cell and glass substrate.

A scan of this size has an acquisition time of approximately 30 min. Figure 4e,f shows the change in SICM and SECM currents, respectively, across the entire scan. The ionic current (SICM, Figure 4e) drifts from 835 pA to 810 pA, a change of less than  $1 \text{ pA min}^{-1}$ . This has a negligible effect on SICM topography imaging as a percentage feedback value, compared to bulk, is used. Proportionally, there is a more pronounced drift (deterioration) of the SECM current (Figure 4f) with time, from 10 pA to 6 pA. This makes the self-referencing method described above crucial to the reasonable interpretation of the SECM current data. It should be noted that the spikes both above and below the main trend in Figure 4f are approaches over glass and the root hair cell, respectively; the bulk current is given by the red line.

No interpolation has been applied to the data in Figure 4b,c, and each pixel represents a quantified measurement of the interfacial uptake rate on the nanoscale. Furthermore, it should be noted that much of the scan time is spent in the probe retracting over a sufficient distance to map out topography of the root hair cell on the glass substrate. Many adherent mammalian cells are less than  $1 \mu\text{m}$  in height and thus the scan could be acquired significantly faster in future experiments. Moreover, faster piezoelectric positioning systems would further reduce the scan time and increase pixel density.

**Differentiation of Subcellular Uptake Heterogeneities.** While the ability to distinguish between uptake and no uptake was an important validation of the method, the technique was also applied to differentiate between the uptake rates across a single cell. Figure 5a shows a single *Zea mays* root hair cell, curved in a hairpin shape (bend outside of the optical micrograph) such that the root hair body and root hair tip could be imaged concurrently. The topography from the scan

area denoted by the dashed white box in Figure 5a is shown in Figure 5b. The two areas of the cell are at different heights above the glass substrate but both suggest the cylindrical shape seen in Figure 4.

The normalized SECM current map (Figure 5c, response over the background glass slide grayed out to emphasize contrast; see Supporting Information, section SI-4 for raw data) shows two clearly defined regions, labeled “Tip” and “Body” on Figure 5b, that have different normalized SECM current value ranges. The body of the cell generally has higher normalized SECM current values (mean = 0.956; standard deviation (s.d.) = 0.033) than at the cell tip (mean = 0.922, s.d. = 0.034), suggesting a faster uptake rate at the root hair tip than at the cell body. This difference between the two regions is emphasized when the data are displayed as a histogram (Figure 5d), where the bell-shaped spread of the normalized SECM current values at the tip is shifted from that of the body. The function of the root hair cell is to uptake nutrients that can then be distributed to the rest of the plant,<sup>45</sup> and the higher level of uptake at the tip of the cell could potentially be a result either of a higher density of membrane transport proteins or a generally looser membrane in this region. However, the higher uptake could also be caused by the charge density, arising as a result of charged proteins and lipids at the cell surface. Recent work with SICM for charge mapping<sup>33</sup> has shown that the tip of a root hair cell carries a significant negative charge when compared to the cell body and this could play an important role in the uptake of the positively charged  $[\text{Ru}(\text{NH}_3)_6]^{3+}$  analyte used.

Despite the difference in overall uptake rates between the two regions, there is a spread of uptake values that can be attributed to several factors. First, heterogeneities in protein or charge lipid distribution on the cell surface would cause a distribution of uptake rates (normalized SECM current). A second reason is that the SECM currents measured during the experiment are rather small ( $\sim 10 \text{ pA}$ ) and thus there will be a natural variation as a result of electrical noise. With these limitations in mind, it is possible to quantify the normalized

SECM current values measured at both the tip and the body using the simulated calibration curve (Figure 3c). The mean values stated above correspond to an uptake rate of  $0.27 \pm 0.05 \text{ cm s}^{-1}$  for the cell tip and  $0.22 \pm 0.05 \text{ cm s}^{-1}$  for the cell body. The ability to distinguish between two regions with similar uptake rates suggests this technique has great promise going forward.

## CONCLUSION

We have demonstrated the use of dual-barrel SICM-SECM nanoprobe to simultaneously measure the topography and spatially resolve the uptake rate of a molecule of interest delivered from the probe across an interface. As a proof of concept, the uptake of hexaammineruthenium(III) to *Zea mays* root hair cells was studied, highlighting heterogeneities in uptake rate across a single cell, with a slightly higher rate of analyte uptake at the cell tip than at the cell body based on the probe current response. These qualitative differences were then quantified using FEM simulations of the experimental setup to provide a powerful platform for mapping and quantifying the uptake rate of electroactive species across an interface. A key feature of the approach has been pixel-level self-referencing of both the SICM and SECM response at each point in a map to overcome any drift in the response of the two channels.

This new technique could aid the screening of drug molecules; for example, using this assay in tandem with cytotoxicity experiments to inform the user of the efficacy of the drug once it had crossed the cell membrane. The technique could also be used to study electrocatalysis and other materials reactivity problems. This work adds significant new functionality to the family of scanning electrochemical probe techniques and could be combined with laser-scanning confocal microscopy and other microscopies to investigate a wide range of processes, from biological (living) systems to materials and catalysis.

## ASSOCIATED CONTENT

### Supporting Information

The Supporting Information is available free of charge on the ACS Publications website at DOI: 10.1021/acs.analchem.6b04629.

Full description of the geometry and conditions of the FEM simulations, a justification of the probe-substrate deduced from those simulations, a justification of the use of steady-state simulations, and the raw normalized current data from Figure 5(PDF)

## AUTHOR INFORMATION

### Corresponding Author

\*E-mail: p.r.unwin@warwick.ac.uk.

### ORCID

Ashley Page: 0000-0001-7233-6337

### Notes

The authors declare no competing financial interest.

## ACKNOWLEDGMENTS

This work was supported by the EPSRC through the MOAC DTC, Grant No. EP/F500378/1 (A.P.), the University of Warwick Chancellor's International Scholarship (M.K.), and the European Research Council (Grant ERC-2009-AdG 247143-QUANTIF) (A.A. and P.R.U.). This work was funded

in part by a Leverhulme Trust Research Project Grant (D.P.). The authors would like to thank Dr. Alex Colburn for the custom-built electronic equipment used in this work.

## REFERENCES

- (1) Alberts, B.; Johnson, A.; Lewis, J.; Morgan, D.; Raff, M.; Roberts, K.; Walter, P. *Molecular Biology of the Cell*, 6th ed.; Garland Science: New York, 2014.
- (2) Lobritz, M. A.; Belenky, P.; Porter, C. B. M.; Gutierrez, A.; Yang, J. H.; Schwarz, E. G.; Dwyer, D. J.; Khalil, A. S.; Collins, J. J. *Proc. Natl. Acad. Sci. U. S. A.* **2015**, *112* (27), 8173–8180.
- (3) Wikström, M.; Sharma, V.; Kaila, V. R. I.; Hosler, J. P.; Hummer, G. *Chem. Rev.* **2015**, *115* (5), 2196–2221.
- (4) Hunter, C. A.; Jones, S. A. *Nat. Immunol.* **2015**, *16* (5), 448–457.
- (5) Calatayud, M. P.; Sanz, B.; Raffà, V.; Riggio, C.; Ibarra, M. R.; Goya, G. F. *Biomaterials* **2014**, *35* (24), 6389–6399.
- (6) Zhou, J.; Li, D.; Su, C.; Wen, H.; Du, Q.; Liang, D. *Phys. Chem. Chem. Phys.* **2015**, *17* (14), 8653–8659.
- (7) Cho, E. C.; Zhang, Q.; Xia, Y. *Nat. Nanotechnol.* **2011**, *6* (6), 385–391.
- (8) Hasegawa, P. M. *Environ. Exp. Bot.* **2013**, *92*, 19–31.
- (9) Stein, W. D.; Litman, T. *Channels, Carriers, and Pumps: An Introduction to Membrane Transport*, 2nd ed.; Elsevier: Amsterdam, The Netherlands, 2014.
- (10) Grever, C.; Gameiro, A.; Mager, T.; Fendler, K. *Annu. Rev. Biophys.* **2013**, *42*, 95–120.
- (11) Passarelli, M. K.; Newman, C. F.; Marshall, P. S.; West, A.; Gilmore, I. S.; Bunch, J.; Alexander, M. R.; Dollery, C. T. *Anal. Chem.* **2015**, *87* (13), 6696–6702.
- (12) Rezgui, R.; Blumer, K.; Yeoh-Tan, G.; Trexler, A. J.; Magzoub, M. *Biochim. Biophys. Acta, Biomembr.* **2016**, *1858* (7), 1499–1506.
- (13) Wang, T.; Bai, J.; Jiang, X.; Nienhaus, G. U. *ACS Nano* **2012**, *6* (2), 1251–1259.
- (14) Tsang, C. N.; Ho, K. S.; Sun, H.; Chan, W. T. *J. Am. Chem. Soc.* **2011**, *133* (19), 7355–7357.
- (15) Kang, M.; Momotenko, D.; Page, A.; Perry, D.; Unwin, P. R. *Langmuir* **2016**, *32*, 7993–8008.
- (16) Kwak, J.; Bard, A. J. *Anal. Chem.* **1989**, *61*, 1794–1799.
- (17) Hansma, P. K.; Drake, B.; Marti, O.; Gould, S. A.; Prater, C. B. *Science* **1989**, *243* (4891), 641–643.
- (18) Shevchuk, A. I.; Frolenkov, G. I.; Sanchez, D.; James, P. S.; Freedman, N.; Lab, M. J.; Jones, R.; Klenerman, D.; Korchev, Y. E. *Angew. Chem., Int. Ed.* **2006**, *45* (14), 2212–2216.
- (19) Happel, P.; Thatenhorst, D.; Dietzel, I. D. *Sensors* **2012**, *12* (11), 14983–15008.
- (20) Bergner, S.; Vatsyayan, P.; Matysik, F. *Anal. Chim. Acta* **2013**, *775*, 1–13.
- (21) Schulte, A.; Nebel, M.; Schuhmann, W. *Annu. Rev. Anal. Chem.* **2010**, *3*, 299–318.
- (22) Filice, F. P.; Li, M. S. M.; Ding, Z. *Anal. Chim. Acta* **2016**, *908*, 85–94.
- (23) Bondarenko, A.; Lin, T.-E.; Stupar, P.; Lesch, A.; Cortes-Salazar, F.; Girault, H. H.; Pick, H. M. *Anal. Chem.* **2016**, *88* (23), 11436–11443.
- (24) Gonsalves, M.; Barker, A. L.; Macpherson, J. V.; Unwin, P. R.; Hare, D. O.; Winlove, C. P. *Biophys. J.* **2000**, *78*, 1578–1588.
- (25) Armstrong-James, M.; Millar, J.; Kruk, Z. L. *Nature* **1980**, *288*, 181–183.
- (26) Herr, N. R.; Kile, B. M.; Carelli, R. M.; Wightman, R. M. *Anal. Chem.* **2008**, *80* (22), 8635–8641.
- (27) Comstock, D. J.; Elam, J. W.; Pellin, M. J.; Hersam, M. C. *Anal. Chem.* **2010**, *82* (4), 1270–1276.
- (28) Takahashi, Y.; Shevchuk, A. I.; Novak, P.; Murakami, Y.; Shiku, H.; Korchev, Y. E.; Matsue, T. *J. Am. Chem. Soc.* **2010**, *132* (29), 10118–10126.
- (29) O'Connell, M. A.; Wain, A. J. *Anal. Chem.* **2014**, *86* (24), 12100–12107.



- (30) Morris, C. A.; Chen, C.-C.; Baker, L. A. *Analyst* **2012**, *137* (13), 2933–2938.
- (31) Takahashi, Y.; Shevchuk, A. I.; Novak, P.; Zhang, Y.; Ebejer, N.; MacPherson, J. V.; Unwin, P. R.; Pollard, A. J.; Roy, D.; Clifford, C. A.; Shiku, H.; Matsue, T.; Klenerman, D.; Korchev, Y. E. *Angew. Chem., Int. Ed.* **2011**, *50* (41), 9638–9642.
- (32) O’Connell, M. A.; Lewis, J. R.; Wain, A. J. *Chem. Commun.* **2015**, *51* (51), 10314–10317.
- (33) Perry, D.; Paulose Nadappuram, B.; Momotenko, D.; Voyias, P. D.; Page, A.; Tripathi, G.; Frenguelli, B. G.; Unwin, P. R. *J. Am. Chem. Soc.* **2016**, *138* (9), 3152–3160.
- (34) Nadappuram, B. P.; McKelvey, K.; Al Botros, R.; Colburn, A. W.; Unwin, P. R. *Anal. Chem.* **2013**, *85* (17), 8070–8074.
- (35) Ebejer, N.; Güell, A. G.; Lai, S. C. S.; McKelvey, K.; Snowden, M. E.; Unwin, P. R. *Annu. Rev. Anal. Chem.* **2013**, *6*, 329–351.
- (36) Güell, A. G.; Cuharuc, A. S.; Kim, Y. R.; Zhang, G.; Tan, S. Y.; Ebejer, N.; Unwin, P. R. *ACS Nano* **2015**, *9* (4), 3558–3571.
- (37) Takahashi, Y.; Murakami, Y.; Nagamine, K.; Shiku, H.; Aoyagi, S.; Yasukawa, T.; Kanzaki, M.; Matsue, T. *Phys. Chem. Chem. Phys.* **2010**, *12* (34), 10012–10017.
- (38) Perry, D.; Momotenko, D.; Lazenby, R. A.; Kang, M.; Unwin, P. R. *Anal. Chem.* **2016**, *88* (10), 5523–5530.
- (39) Chen, C.-C.; Zhou, Y.; Baker, L. A. *Annu. Rev. Anal. Chem.* **2012**, *5* (1), 207–228.
- (40) Edwards, M. A.; Williams, C. G.; Whitworth, A. L.; Unwin, P. R. *Anal. Chem.* **2009**, *81* (11), 4482–4492.
- (41) Sa, N.; Baker, L. A. *J. Am. Chem. Soc.* **2011**, *133* (27), 10398–10401.
- (42) Sa, N.; Lan, W. J.; Shi, W.; Baker, L. A. *ACS Nano* **2013**, *7* (12), 11272–11282.
- (43) Perry, D.; Al Botros, R.; Momotenko, D.; Kinnear, S. L.; Unwin, P. R. *ACS Nano* **2015**, *9* (7), 7266–7276.
- (44) Chen, C.-C.; Baker, L. A. *Analyst* **2011**, *136* (1), 90–97.
- (45) Foster, K. J.; Miklavcic, S. J. *Front. Plant Sci.* **2016**, *7*, 914.